

The neutron star inner crust and symmetry energy

Fabrizio Grill and Constança Providência
*Centro de Física Computacional, Department of Physics,
University of Coimbra, P-3004-516 Coimbra, Portugal*

Sidney S. Avancini

Depto de Física - CFM - Universidade Federal de Santa Catarina Florianópolis - SC - CP. 476 - CEP 88.040 - 900 - Brazil

The cell structure of clusters in the inner crust of a cold β -equilibrium neutron star is studied within a Thomas Fermi approach and compared with other approaches which include shell effects. Relativistic nuclear models are considered. We conclude that the symmetry energy slope L may have quite dramatic effects on the cell structure if it is very large or small. Rod-like and slab-like pasta clusters have been obtained in all models except one with a large slope L .

I. INTRODUCTION

The inner crust of a neutron star lies between the neutron drip density ($\rho_d \approx 3 \times 10^{-4} \text{ fm}^{-3}$), defined as the density where the neutrons start to drip out from the nuclei of the crust, and the crust-core transition density ($\rho \approx 8 \times 10^{-2} \text{ fm}^{-3}$). In this region matter is most probably formed by a lattice of heavy and neutron rich nuclei immersed in a sea of superfluid neutrons and ultrarelativistic electrons. Complex structures (e.g. rods and slabs) are expected to be formed in the bottom part of the inner crust, the so-called pasta phase region, where the transition to the homogeneous core matter occurs.

The first microscopic calculation of the inner crust structure was performed by Negele and Vautherin in 1973 [1]. In this work, which is still used as a benchmark in neutron star calculations, the inner crust was studied in the Wigner-Seitz approximation, which divides the lattice in independent spherical cells each with the nucleus in the center surrounded by the electron and neutron gases. Nuclear matter was described with the Hartree-Fock (HF) approximation based on the Density Matrix Expansion [2]. The parameters of that model were adjusted to reproduce the experimental binding energies of atomic nuclei and theoretical calculations of infinite neutron matter. The inner crust matter calculated in that work has for each cell a magic or semi-magic proton number (i.e. $Z = 40$ and $Z = 50$), indicating that in these calculations there are strong proton shell effects, as in isolated atomic nuclei.

Later Douchin and Haensel proposed a new study where the neutron star structure was calculated using the same Equation of State (EOS) in the whole star, from the outer crust to the core [3]. In that work nuclear matter was treated in the Wigner-Seitz (WS) approximation using the non-relativistic Compressible Liquid Drop (CLD) model and the SLy4 effective interaction [4]. The shell effects were neglected both for protons and neutrons. In the transition between the inner crust and the core five different pasta shapes were considered: spherical nuclei (droplets), cylinders of nuclear matter (rods), and plane slabs of nuclear matter (slabs) in a neutron gas, as well as cylindrical holes (tubes) and spherical holes (bubbles)

in nuclear matter filled with a neutron gas. Within that model these authors found that in the whole inner crust the shape that minimizes the energy is the droplet and that those cells were characterized by a weak change in the proton number: from $Z \approx 40$ near the neutron drip to $Z \approx 50$ in the region of the transition to the core. Moreover because of the absence of proton shell effects in all the calculated configurations the proton number was not magic or semi-magic.

The effect of pairing correlations on the structure of WS cells was investigated for the first time in [5] within the Hartree-Fock-Bogoliubov approach (HFB). In the most recent version of these calculations these authors solved the HFB equations using an equation of state (EOS) mixture of the phenomenological functional of Fayans et al [6], employed in the nuclear cluster region, and a microscopical functional derived from Bruckner-Hartree-Fock calculations in infinite neutron matter. In this framework it was found that the cells have not a magic or semi-magic number of protons and that pairing can change significantly the structure of the cells compared to HF calculations.

The pairing effect was also studied by Gögelein and Mütter in 2007 [7]. In this work these authors used a self-consistent Skyrme-Hartree-Fock (SHF) approach in order to study the cell structure in the pasta phase region ($0.01 \text{ fm}^{-3} < \rho < 0.1 \text{ fm}^{-3}$), where three different pasta shapes were considered: droplet, rod and slab. The pairing correlations were evaluated within the BCS approach, assuming a density-dependent contact interaction, while, for the nuclear interaction, the SLy4 parametrization [4] was used. Contrary to what was obtained in [3] in this work the calculations showed that all the three cell shapes appear in the inner crust before the transition to the homogeneous core. Moreover the calculated core-crust transition density was coherent with the value that was found in [8] for the SLy4 interaction within a dynamical spinodal calculation.

Recently Grill et al. proposed a new inner crust structure calculation based on the HFB approach [9]. This study was performed in the regions which are supposed to be formed by a lattice of spherical clusters. Thus the inner crust matter was divided in spherical cells treated

in the Wigner-Seitz approximation and the structure of these cells (i.e. neutron number (N), proton number (Z) and cell radius (R_{ws})) were obtained from the energy minimization at beta equilibrium. For the HFB calculations it was considered a SLy4 interaction [4] in the particle-hole channel, while in the particle-particle channel three zero-range density-dependent pairing forces of various intensities were used. With this model it was possible to find very reliable results in the low density regions of the inner crust. Indeed the calculated structure is coherent with the results of outer crust calculations in the literature (e.g. [10]). Moreover, in those regions a very weak dependence on the pairing interaction was found. On the other hand in the high density regions of the inner crust the imposed discretization of the free neutron gas generates an underestimation of the energy in the smaller cells: it was thus used an empirical correction [11] which, however, was characterized by large fluctuations, so the structure of the cells in those regions was not guaranteed by those calculations.

In this paper we present a calculation of the inner crust structure using a relativistic mean field density dependent Thomas-Fermi approach (TF) [12]. A complete self consistent calculation is performed, namely, no parametrization of the density and surface energy as in [7] has been used. This approach, which neglects the shell effect for both neutrons and protons, is less accurate than the HFB in the low density regions, where the nucleus influences the cell properties. However, in the high density regions, when the free neutron gas becomes more important than the nucleus, the accuracy of the TF approximation can be higher than that of the HFB approach: indeed with this model the discretization of the free neutron gas is not necessary. Moreover, with the HFB approach it is actually possible to consider just the spherical symmetry and so the droplet is the only available shape of the cells. On the other hand with the TF approach it is possible to study also the cylindrical and the plane symmetries, making available also the rod and slab cell shapes: we have performed our study also in the pasta phase region and determined the cell structure until the crust-core transition.

The neutron inner crust is particularly sensitive to the density dependence of the symmetry energy [13], and, therefore, comparing results obtained with different nuclear interactions will show how the symmetry energy affects the cell structure. This comparison is possible within a TF but would be prohibitive within a HFB calculation due to the excessive CPU time required.

II. FORMALISM

We will apply in the present study the self-consistent Thomas-Fermi calculation presented in [12, 14], within relativistic nuclear models with constant couplings and non-linear terms [15], and with density dependent couplings [16]. In the relativistic mean-field theory protons

and neutrons interact with and through an isoscalar-scalar field σ , an isoscalar-vector field ω^μ , an isovector-vector field ρ^μ and an isovector-scalar field δ . Within the first class of models, that we will designate by Non Linear Walecka Models (NLWM), we consider NL3 [17] with non linear σ terms, NL3 $_{\omega\rho}$ including also non-linear $\omega\rho$ terms which allow the modulation of the density dependence of the symmetry energy [18], FSU [19] and IU-FSU [20] with non-linear σ , ω and $\omega\rho$ terms. These two parametrizations were constrained by the collective response of nuclei to the isoscalar monopole giant resonance (ISGMR) and the isovector dipole giant resonance (IVGDR). Within the second class of models with density dependent couplings we consider DD-ME2 [21] and DD-ME δ [22]: DD-ME2, as all the non-linear parametrizations considered, does not include the δ meson, and was adjusted to experimental data based on finite nuclei properties; DD-ME δ contains the δ meson and was fitted to microscopic ab-initio calculations in nuclear matter and finite nuclei properties.

Stellar matter will be described by a mixture of protons, neutrons and electrons in chemical equilibrium. Electrons are described as a relativistic fermion gas which interacts with protons through the electromagnetic field A^μ .

All the equations that allow the performance of the Thomas-Fermi calculation are derived from the Lagrangian density

$$\mathcal{L} = \sum_{i=p,n} \mathcal{L}_i + \mathcal{L}_e + \mathcal{L}_\sigma + \mathcal{L}_\omega + \mathcal{L}_\rho + \mathcal{L}_\delta + \mathcal{L}_\gamma + \mathcal{L}_{nl}, \quad (1)$$

where the nucleon Lagrangian reads

$$\mathcal{L}_i = \bar{\psi}_i [\gamma_\mu i D^\mu - M^*] \psi_i, \quad (2)$$

with

$$iD^\mu = i\partial^\mu - \Gamma_\omega \Omega^\mu - \frac{\Gamma_\rho}{2} \boldsymbol{\tau} \cdot \boldsymbol{\rho}^\mu - e \frac{1+\tau_3}{2} A^\mu, \quad (3)$$

$$M^* = M - \Gamma_\sigma \sigma - \Gamma_\delta \boldsymbol{\tau} \cdot \boldsymbol{\delta}, \quad (4)$$

and the electron Lagrangian is given by

$$\mathcal{L}_e = \bar{\psi}_e [\gamma_\mu (i\partial^\mu + eA^\mu) - m_e] \psi_e. \quad (5)$$

The meson and electromagnetic Lagrangian densities are

$$\mathcal{L}_\sigma = \frac{1}{2} (\partial_\mu \sigma \partial^\mu \sigma - m_\sigma^2 \sigma^2)$$

$$\mathcal{L}_\omega = \frac{1}{2} \left(-\frac{1}{2} \Omega_{\mu\nu} \Omega^{\mu\nu} + m_\omega^2 \omega_\mu \omega^\mu \right)$$

$$\mathcal{L}_\rho = \frac{1}{2} \left(-\frac{1}{2} \mathbf{R}_{\mu\nu} \cdot \mathbf{R}^{\mu\nu} + m_\rho^2 \boldsymbol{\rho}_\mu \cdot \boldsymbol{\rho}^\mu \right)$$

$$\mathcal{L}_\delta = \frac{1}{2} (\partial_\mu \delta \partial^\mu \delta - m_\delta^2 \delta^2)$$

$$\mathcal{L}_\gamma = -\frac{1}{4} F_{\mu\nu} F^{\mu\nu}$$

$$\begin{aligned} \mathcal{L}_{nl} = & -\frac{1}{3!} \kappa \sigma^3 - \frac{1}{4!} \lambda \sigma^4 + \frac{1}{4!} \xi g_\omega^4 (\omega_\mu \omega^\mu)^2 \\ & + \Lambda_\omega \Gamma_\omega^2 \Gamma_\rho^2 \omega_\mu \omega^\mu \boldsymbol{\rho}_\mu \cdot \boldsymbol{\rho}^\mu \end{aligned}$$

where $\Omega_{\mu\nu} = \partial_\mu\omega_\nu - \partial_\nu\omega_\mu$, $\mathbf{R}_{\mu\nu} = \partial_\mu\boldsymbol{\rho}_\nu - \partial_\nu\boldsymbol{\rho}_\mu - \Gamma_\rho(\boldsymbol{\rho}_\mu \times \boldsymbol{\rho}_\nu)$ and $F_{\mu\nu} = \partial_\mu A_\nu - \partial_\nu A_\mu$. The four coupling parameters Γ_σ , Γ_ω , Γ_ρ and Γ_δ of the mesons to the nucleons are density dependent in the relativistic density dependent models considered, namely, DD-ME2 [21] and DD-ME δ [22]. The non-linear term \mathcal{L}_{nl} is absent in these models. In all the other models, NL3 [17], NL3 $_{\omega\rho}$ [18], FSU [19] and IU-FSU [20], the couplings are constants and at least some of the non-linear terms of \mathcal{L}_{nl} are included. In the above Lagrangian density τ is the isospin operator.

The results obtained within the above relativistic mean-field models will be compared with the corresponding results calculated with the non-relativistic effective Skyrme interaction SLy4 [4] within two formalisms: a HFB calculation [9] and a CLD calculation [3]. We will discuss how sensitive is the structure of the non-homogeneous inner-crust of a neutron star to the properties of the EOS and the formalism used. In Table I the saturation nuclear matter properties and the σ meson mass are shown. The σ meson mass has a strong influence on the nuclear surface energy and is included in the table to help the discussion.

In Fig. 1 the symmetry energy and its slope L are plotted for all the models. The models considered have very similar values for the symmetry energy at saturation, namely, between 31.3 and 32.6 MeV except NL3 that has a quite high value, 37.3 MeV. However, there is a larger dispersion of the symmetry energy slope L with values between 45 and 60 MeV, together with 118 MeV for NL3. All models behave in a similar way except NL3 whose slope is much larger above $\rho > \rho_0/3$. SLy4 has the smallest slope L only at saturation density. FSU has the second largest slope only above the density $\rho \sim 0.7\rho_0$. The properties of the pasta will reflect these facts, with IU-FSU and NL3 behaving in a quite different way, while all the other models showing similar results. The slope L has a direct influence on the surface energy tension and surface thickness of the clusters.

A smaller L corresponds generally to a larger surface tension and smaller neutron skin thickness [18] as can be confirmed comparing the surface tensions of the above models. In Fig. 2 the surface tension obtained from the derivatives of the meson fields, as indicated in [23], are plotted. The main differences between the models are due to the properties of the EOS at subsaturation densities: a smaller L dictates a larger surface tension in asymmetric matter: IU-FSU has the smallest L and largest surface tension; it is this effect that explains the difference between NL3 and NL3 $_{\omega\rho}$. The dependence of the surface tension in symmetric nuclear matter on the model properties was well discussed in [24], a smaller incompressibility will give a smaller surface tension: this explains the small DD-ME δ value; a smaller value of m_σ and a larger saturation density will give rise to a larger surface tension as in IU-FSU.

III. RESULTS

In our study of the inner crust structure we have considered three different cell shapes: the droplet, the rod and the slab. In most part of the inner crust, that we will designate by standard inner crust ($\rho \leq 4.71 \times 10^{-2} \text{ fm}^{-3}$), we have limited our study just to the droplet configuration, so, as in [1, 9], the lattice structure is described as a set of spherical cells, with radius R_{ws} , treated in the Wigner-Seitz approach. The volume of a spherical cell with radius R_{ws} is

$$V^d(R_{ws}) = \frac{4}{3}\pi R_{ws}^3. \quad (6)$$

However in the higher density regions, that we will designate by pasta phase regions ($\rho \geq 4.71 \times 10^{-2} \text{ fm}^{-3}$), we have taken into account all the three shapes. Rod cells have cylindrical shape with the radius R_{ws} and length set for simplicity to $l = 30 \text{ fm}$, which is $\sim 1.5 R_{ws}$ in region 1 (the final results are independent of this parameter)

$$V^r(R_{ws}) = l\pi R_{ws}^2. \quad (7)$$

Slab cells have the shape of a parallelepiped with width and length set to $l = 30 \text{ fm}$ (the final results are independent on this parameter, too) and depth equal to $2R_{ws}$, so that

$$V^s(R_{ws}) = 2l^2 R_{ws}. \quad (8)$$

We consider these three different cell shapes at a given density and calculate the cell structure through the minimization of the energy per baryon under the condition of β -equilibrium. For a fixed number of protons and neutrons at a given density it is possible to obtain univocally the cell radius (R_{ws})

$$V^i(R_{ws}) = \frac{N+Z}{\rho} \quad i = d, r, s, \quad (9)$$

and by the β -equilibrium condition for each proton number it is possible to calculate the neutron number. Finally the cell structure is univocally defined searching the cell shape and the proton number that minimize the energy per baryon. In this minimization process we have treated Z and N as an integer (contrary to the approach of Douchin and Haensel [3]). The main effects of imposing this condition are: smaller Wigner-Seitz cells and larger energies are obtained.

In particular for each fixed density we have calculated the cell shape, the proton and neutron number, the cell radius (R_{ws}), which is defined from the cell volume (6), (7) and (8), the energy per baryon (E/A), the neutron chemical potential (μ_N) and the proton fraction ($x = Z/(Z+N)$).

A. Standard inner crust

The properties of the standard inner crust are reported in the Tables II and III where the proton number, neutron

number, Wigner-Seitz radius, energy per baryon, neutron chemical potential and total proton fraction defined for twelve different values of the density defined in the second line of these tables. The first ten were introduced by Negele and Vautherin in [1] and we have added two more at low densities. In the following, we identify these densities by a label from 1 (high density close to the crust-core transition) to 12 (low density below neutron drip) and will refer to twelve density regions. In Fig. 3 and in Fig. 4 we plot some of the properties of the Wigner-Seitz cells as a function of density. In particular, in Fig. 3 we show the neutron density at the cell center and the cell border, the cluster proton fraction at the cluster center and the neutron skin thickness $\Theta = R_n - R_p$, with $R_i^2 = 5/3 < r_i^2 >$, and in Fig. 4, we plot the Wigner-Seitz proton number Z , neutron number N , radius R_{ws} , total proton fraction x , droplet number A and droplet proton fraction Z/A . The droplet nucleon number A has been estimated from the radius R_{ws} and the neutron density at R_{ws} , namely, $A = Z + N[1 - V^i(R_{ws})\rho_N(R_{ws})]$. Whenever available data from [1, 3, 9] have been included for comparison. In order to better understand the behaviour of the NL3 interaction we have added some points at high density (regions from 1 to 3).

The main differences occur above $\rho = 0.02 - 0.05 \text{ fm}^{-3}$. Below this density, except for the IU-FSU and NL3, all TF results lie between an upper and lower bound defined by the HFB and HF calculations. Above $\rho = 0.05 \text{ fm}^{-3}$ non-spherical geometries may arise with lower energy within the TF calculation, and this explains partially the differences. The CLD calculation for the SLy4 interaction of [3] also follows the main trend obtained with the relativistic models.

We will first discuss the proton number as a function of density. Different properties of the models explain the existing differences in the results. NL3 and IU-FSU have, respectively, the smallest and largest proton number. This is a clear effect of the slope L , the large value of NL3 and the small value of IU-FSU, and corresponding surface tensions: in IU-FSU neutrons do not drip out so easily, the central droplet density is larger, and according to the liquid droplet model [25], the proton number increases with the surface energy; the opposite occurs with NL3. NL3 $_{\omega\rho}$ only differs from NL3 in the isospin channel: a larger L clearly gives a larger proton number. The interaction DD-ME δ has, next to NL3, the smallest proton number and Wigner-Seitz radius in a large part of the density range considered, due to a smaller surface energy at large proton fraction which favors smaller droplets. FSU has a larger effective nucleon mass at saturation than all the other models, except IU-FSU. In [24] it was shown that a larger effective mass favors a smaller surface thickness and, therefore, a larger nucleon number inside the droplet is expected, including a larger proton number.

The results reported in Table II show that in the TF calculations the proton number does not change considerably close to the transition to the outer crust and lies

between 39 and 46. The proton number found with the HFB calculations converges to values around $Z = 36$, which is the proton number that characterizes the nuclei at the drip density (e.g. [10]). This shell effect can not be reproduced by the TF calculations. The proton number obtained using the DD-ME2, DD-ME δ , NL3 $_{\omega\rho}$ and FSU show a similar behaviour to the one found in [3], where shell effects are also neglected: below $\rho \sim 10^{-3} \text{ fm}^{-3}$ all these models predict a larger proton number than the HFB [9] or the HF [1] calculations. This results are also similar to the ones calculated in [26] within the liquid drop model or in [27] within a TF calculation with energy density functionals constructed in order to reproduce nuclear matter properties. In this last work it is seen that Z is sensitive to the properties of the EOS. On the other hand in [28], a relativistic Brueckner-Hartree-Fock calculation was performed and quite small proton numbers were obtained, very similar to NL3. Our results also agree with the conclusions of [13] where, within a Thomas Fermi calculation applied to a macroscopic nuclear model, it was shown that the proton number is larger for smaller values of L .

In regions 1 and 2 the proton number found with the TF calculations has a consistent drop (Fig. 4). This is a behaviour also occurring in other works (e.g. [1], [5], [28] and [3]) and it is related with both the decrease of the Wigner-Seitz radius and the increase of the volume occupied with nuclear matter.

The neutron numbers obtained with all interactions are very similar below $\rho \sim 5 \times 10^{-3} \text{ fm}^{-3}$ and they are comparable to the ones calculated within the HFB [9] and HF [1] calculations where shell effects are included, (see Table II and Fig. 4). Above $\rho \sim 5 \times 10^{-3} \text{ fm}^{-3}$ model properties explain the existing differences.

NL3 and DD-ME δ interaction give neutron numbers smaller than the other interactions (except for NL3 in region 2). The neutron numbers found with NL3 $_{\omega\rho}$ (in the regions 1 and 2) and IU-FSU (in the region 1) are higher than what has been found with the other interactions. In fact, IU-FSU predicts the rod shape in region 1. If the droplet shape would have been considered in this region for IU-FSU the cells would have been characterized by $Z = 102$, $N = 2066$ and $R_{ws} = 22.2 \text{ fm}$, much bigger than what has been found with all the other interactions. As a whole the neutron number calculated in all the considered interactions is coherent with the results found in the literature. It increases consistently with the density and only at very high density does it decrease, as found in [3], [9] and [1]. We conclude that, as expected, the neutron number is not strongly linked to the shell effect.

The TF and HFB neutron numbers are very similar just in the middle density range (corresponding to regions 5, 6 and 7). For larger densities (regions 2, 3 and 4) the neutron numbers found with the HFB calculations are lower. Only in the region 3 the neutron numbers are similar, but this is a consequence of a big difference on the proton number. Finally, as expected, an impor-

tant difference with respect to [9] occurs in the low density regions. As also found with the proton number, the HFB results converge to the closed shell neutron number ($N = 82$) which characterizes the neutron drip density and the initial part of the outer crust (e.g. [10]), while the TF calculations, which does not include shell effects, cannot reproduce this behaviour. Furthermore, looking at the neutron chemical potential (Tab. III), we conclude that the neutron drip occurs above region 10 in the HFB calculations, due to the shell effects, while the TF calculations predict this transition in the region 12, which is characterized by quite low density. However, with the NL3 parametrization we have found a drip density similar to that found with the HFB calculations. TF results are very similar to those found by Negele and Vautherin [1]: only at the very high density (regions 1 and 2) there is a difference and the neutron number found in [1] is much larger than that found with TF.

The cell neutron number is closely linked to the radius of the Wigner-Seitz cells (Tab. II and Fig. 4). The cell radius is quite independent on the nuclear interaction and the qualitative behaviour obtained in the TF calculation is equal to what has been found with HFB [9] and HF [1]. Some quantitative differences identified are: a) the cells calculated with NL3 and DD-ME δ interaction are slightly smaller than those found with all the other interactions, which is coherent with the smaller neutron number predicted by these interactions (only region 2 is out of this trend in NL3); b) as with the neutron number the cell radius obtained using the TF and HFB approach are very similar in the middle density regions (from 5 to 7) but differ in the low and high density ranges, where the HFB radius is smaller.

In region 1, the lowest energy cell shape predicted by IU-FSU is the rod and, as it will be described in the next section, a change in the cell shape is always correlated with a drop in the value of the cell radius (Fig. 5). However, this does not occur in this case because IU-FSU predicts values higher than those found with all the other interactions.

The proton fraction calculated with all interactions is very similar (Tabs. III, VI and Fig. 4). Only the values calculated with the IU-FSU and NL3 interactions are different from the general trend at higher densities (Tab. III in the regions from 1 to 4 and Tab. VI). The behaviour of the proton fraction is similar to those found in the literature [1, 7, 12, 13]: its value decreases with increasing the density until, at high densities close to the crust-core transition, it changes its slope in order to reproduce the correct behaviour of homogeneous matter (Fig. 4). IU-FSU has the largest symmetry energy at $\rho \sim 0.5\rho_0$ which favors isospin symmetry, NL3 has the smallest symmetry energy which favors a smaller proton fraction. In general a larger symmetry energy favors matter with a smaller isospin asymmetry. This is true for homogeneous matter, but the discussion of non-homogenous matter requires care: properties of clusters are closely dependent on the surface energy which defines how favorable is the creation

of clusters.

The proton fractions obtained in [12] and [7] for the RMF model are smaller than the ones obtained in the present model, except for the NL3 parametrization. This is mainly due to the characteristics of the RMF used: both of them have a large symmetry energy slope at saturation and therefore, a smaller symmetry energy at sub-saturation densities, which favors large isospin asymmetries. Similar results have been obtained in [29]. The calculated proton fraction in [7] with the SLy4 parametrization is consistent both with the CLD model and the HFB calculation, which have used the same parametrization, and are just slightly larger than the ones obtained with all the RMF models discussed in the present work except IU-FSU. In [7] it was also shown that the shell effects were not very important and its main effect was to determine a slightly larger proton fraction.

Some properties of the clusters reflect clearly the density dependence of the symmetry energy (see Fig. 3 and 4). The cluster nucleon number above $\rho = 5 \times 10^{-3} \text{ fm}^{-3}$ is correlated with L while below that density it is not very sensitive to the model. The nucleon number of NL3 clusters decreases above 10^{-2} fm^{-3} and at the crust-core transition is less than 100. On the other hand IU-FSU and SLy4, the models with the smallest slopes L , predict clusters with more than 500 nucleons close to the crust-core transition. All the other models predict clusters that do not go beyond 200-250 nucleons.

The cluster proton fraction decreases, as expected, with density and stabilizes around 0.25 for models with $L = 51 - 60 \text{ MeV}$. For both models with the smallest L , IU-FSU and SLy4 it decreases continuously reaching proton fractions below 0.15 while NL3 just before the crust-core transition has a strong increase of Z/A . We note, however, that as expected from the symmetry energy close to saturation, NL3, with the largest symmetry energy, has the largest proton fraction at the center of the cluster, while IU-FSU has the smallest. The droplet overall proton fraction is then defined by the clusters neutron skin (Fig. 3), which is much larger in NL3.

B. Pasta phase regions

The properties of the pasta phase regions of the inner crust are reported in the tables from IV to VII and in Fig. 5 for the relativistic models.

In the pasta phase regions the matter is studied considering the three different cell shapes: the droplet, the rod and the slab. The transition densities between these different shapes are reported in table VII for all interactions. In this table we have also included the results of Ref. [7]. All the three shapes appear in the inner crust except for NL3, which only predicts droplets. These results agree with those of Refs. [12] and [23], where, using the TF approach and the NL3 parametrization, it was predicted that in β -equilibrium condition only the droplet cell shape would appear. Droplets were also the

only configuration obtained in Refs. [3] and [29]. However, contrary to [3] where the CLD was applied, in [7] all the three shapes were obtained with SLy4 using different frameworks, both TF and HF. In [13] it was shown that models with a large L would not predict the existence of pasta shapes in β -equilibrium matter. Thus we expect that the RMF parametrization used in [29] has a large slope L . The IU-FSU shape transitions occur at densities similar to those obtained in [7] for SLy4 within the HF calculation. These two models predict similar values of L .

The crust-core transition densities found in this work, and indicated in Table VII, agree with the ones found in the literature within a dynamical spinodal calculation: SLy4 at $\rho_t = 0.080 \text{ fm}^{-3}$, NL3 at $\rho_t = 0.054 \text{ fm}^{-3}$, DD-ME2 at $\rho_t = 0.072 \text{ fm}^{-3}$, FSU at $\rho_t = 0.074 \text{ fm}^{-3}$ [8], NL3 $_{\omega\rho}$ at $\rho_t = 0.0855 \text{ fm}^{-3}$ [30] and IU-FSU at $\rho_t = 0.087 \text{ fm}^{-3}$ [20]. As expected results from the pasta calculation are just slightly larger. The crust core transition density is expected to occur within the metastable region between the spinodal and the binodal surfaces. However, for very asymmetric matter as β -equilibrium matter, this region is almost nonexistent, since the binodal and the spinodal surfaces are very close. These results confirm the conclusions of reference [23], namely that the estimation of the crust core transition from the dynamical spinodal is a good one.

The proton and neutron numbers as well as the Wigner-Seitz radius in the pasta phase are reported in the tables IV and V and in Fig. 5. Comparing the behavior of the different models we conclude that: a) the NL3 and IU-FSU interactions are quite different from all the others with a much smaller or larger Z , N and R_{ws} . The very different surface energy obtained within these two models explains this difference; b) all the other models behave in a very similar way, and differences may be explained comparing the symmetry energy slopes within the models built using the same formalism, namely NLWM or density dependent hadronic models. A smaller L favors larger Z , N , and R_{ws} in NL3 $_{\omega\rho}$ with respect to FSU. A smaller effective mass and incompressibility in DD-ME δ favors a smaller surface energy and therefore, smaller Z , N , and R_{ws} than in DD-ME2; c) the behavior of the surface energy with the proton asymmetry explains small differences between models. Close to the crust-core transition asymmetries are large and models with larger surface energies will suffer shape transitions at larger densities for similar cell sizes.

At the shape transitions both the protons and neutron numbers have a sudden change because these numbers have a strong dependence on the cell volume (7) and (8) and thus on the parameter l , which has been arbitrary chosen. However this parameter has just an influence on the proton and neutron number values, it cannot change their behaviour or the calculated matter properties, namely their dependence on the density, the proton fraction, the energy per baryon or the chemical potentials. The cell radius decreases until densities close to

a shape transition where it stabilizes or a small increase occurs just before the transition. The shape transition is then characterized by a decrease of cell size. Similar behavior was described in [12, 29].

A comparison with the results already published in the literature is not always possible. Indeed in [9] just the standard inner crust has been studied, while the results found in [1] at very high density are not realistic because the droplet cell shape was imposed. In [7, 12, 29] consistent calculations have been performed, but a detailed description of the cell structure (N, Z and R_{ws}) was not reported. The cell structure has been reported in [3] (Tab. 1 and 2 of Ref. [3]) where it is possible to see that the proton and neutron numbers have a behaviour similar to what has been found with our TF calculations: after an initial increase until quite high densities, then they decrease and finally they grow again until the crust-core transition ($\rho = 7.5959 \times 10^{-2} \text{ fm}^{-3}$). Also the cell radius has a behaviour very similar to the one obtained in this work: it monotonically decreases until densities close to the crust-core transition ($\rho = 7.0154 \times 10^{-2} \text{ fm}^{-3}$), then it grows until the transition.

One interesting conclusion is that, except for NL3, all the models studied predict slab like configurations in β -equilibrium matter. According to [31] low energy collective modes with an important contribution to the specific heat could be excited in these 'lasagna'-like pastas.

The density in which non-spherical shapes appear was discussed in [25], and an estimation of a nuclear filling fraction of 1/8 was obtained. If no dripped neutrons occur this fraction translates into a average cell density of $n_i/8$, where n_i is the central density of the droplet. However, this density will be larger if the dripped-neutron density is non zero. In fact, we confirm that the models with the lowest rod shape onset have the smallest neutron density at the cell border. This density is closely correlated with the slope L , with a smaller L corresponding to a smaller neutron density. NL3 is an exception because the crust-core transition occurs below this limit. The onset of the slab geometry between different models follows a behavior similar to the rod onset.

IV. CONCLUSIONS

We have studied the inner crust properties of neutron stars within a self-consistent Thomas Fermi approach developed in [12, 14] for relativistic nuclear models. Several relativistic nuclear models have been used both with non linear meson terms and constant couplings, and with density dependent coupling constants. The results have been compared with calculations obtained within the HFB, and the HF [1, 7, 9] formalisms, with the compressible liquid drop model [3] and with a macroscopic nuclear model [13].

It has been shown that the main properties of the Wigner-Seitz cells obtained within the HFB and HF formalisms are reproduced, namely, the average proton

number and the neutron number and the Wigner-Seitz cell radius. As expected, proton shell effects are missing.

The properties of the models used are reflected on the cluster structure. It was seen that a small symmetry energy slope L gave rise to larger cells, with a larger proton and neutron number, while the opposite occurs for a large L . Models with a similar symmetry energy ($\sim 31 - 32$ MeV) and slope L ($\sim 50 - 60$) at saturation density were shown to behave in a similar way, both in the droplet phase and the pasta phase regions. On the other hand models like NL3, with a very large symmetry energy and slope L and IU-FSU, with a quite small L , have shown quite different behaviors. NL3 did not present any pasta phases in the inner crust of β -equilibrium matter, and predicted the smallest proton and neutron numbers, and Wigner-Seitz radius in almost all the inner crust range of densities. On the other hand, IU-FSU predicts a quite low density for the onset of the pasta phase, where all the other models still predict the existence of droplets. The occurrence of the slab shape occurs at a lower densities than in all the other models. However, the IU-FSU crust-core transition density is the largest one and above 0.01 fm^{-3} IU-FSU presents the largest clusters with more than the double of nucleons. All the models, except NL3, predict the existence of slab like configurations in β -equilibrium matter. These 'lasagna'-like structures may

have an important contribution to the specific heat of the crust [31].

The size and composition of the clusters will have an important effect on the transport properties of the crust. In [32] it was shown how the pasta structures could affect the neutrino transport, namely a more uniform distribution of matter, as occurs in NL3 with a larger neutron drip, or a larger range with non-spherical pasta structures could reduce the cross section for elastic neutrino scattering from pasta phases via weak neutral current, and therefore the neutrino opacity.

The effect of the pairing correlations, which were missing in the present work, on the inner crust clusters and the effect of the size and composition of the clusters on the transport properties of the crust will be investigated.

Acknowledgments

This work has been partially supported by QREN/FEDER, the Programme COMPETE, and FCT (Portugal) under the projects PTDC/FIS/113292/2009 and CERN/FP/116366/2010, by the Capes/FCT n. 232/09 bilateral collaboration and by COMPSTAR, an ESF Research Networking Programme.

-
- [1] J. N. Negele, and D. Vautherin, Nucl. Phys. A, 207, 298 (1973).
- [2] J. N. Negele, and D. Vautherin, Nucl. Phys. C, 5, 1472 (1972).
- [3] F. Douchin, and P. Haensel, A&A, 380, 157 (2001).
- [4] E. Chabanat, P. Bonche, P. Haensel, J. Meyer, and R. Schaeffer, Nucl. Phys. A, 623, 710 (1997).
- [5] M. Baldo, U. Lombardo, E. E. Saperstein, and S. V. Tolokonnikov, Nucl. Phys. A, 750, 409 (2005); M. Baldo, E. E. Saperstein, and S. V. Tolokonnikov, Eur. Phys. J. A, 32, 97 (2007).
- [6] S. A. Fayans, S. V. Tolokonnikov, E. L. Trykov, and D. Zaisha, Nucl. Phys. A, 676, 49 (2000).
- [7] P. Gögelein and H. Mütter, Phys. Rev. C, 76, 024312 (2007).
- [8] C. Ducoin, J. Margueron, C. Providência and I. Vidaña, Phys. Rev. C, 83, 045810 (2011).
- [9] F. Grill, J. Margueron, and N. Sandulescu, Phys. Rev. C, 84, 065801 (2011).
- [10] X. Roca-Maza, J. Piekarewicz, T. García-Gálvez, and M. Centelles, arXiv:1109.3011.
- [11] J. Margueron, N. Van Giai and N. Sandulescu, 2007, Proceeding of the International Symposium EXOCT07, "Exotic States of Nuclear Matter", Edited by U. Lombardo et al., World Scientific; arXiv:0711.0106.
- [12] S. S. Avancini, D. P. Menezes, M. D. Alloy, J. R. Marinelli, M. M. W. de Moraes and C. Providência, Phys. Rev. C, 78, 015802 (2008).
- [13] K. Oyamatsu and K. Iida, Phys. Rev. C 75, 015801 (2007).
- [14] S. S. Avancini, L. Brito, J. R. Marinelli, D. P. Menezes, M. M. W. de Moraes, C. Providência, and A. M. Santos, Phys. Rev. C 79, 035804 (2009).
- [15] J. Boguta and A. R. Bodmer, Nucl. Phys. A 292, 413 (1977).
- [16] S. Typel and H. H. Wolter, Nucl. Phys. A656, 331 (1999).
- [17] G. A. Lalazissis, J. König, and P. Ring, Phys. Rev. C 55, 540 (1997).
- [18] C. J. Horowitz and J. Piekarewicz, Phys. Rev. Lett. 86, 5647 (2001); C. J. Horowitz and J. Piekarewicz, Phys. Rev. C 64, 062802 (2001).
- [19] B. G. Todd-Rutel and J. Piekarewicz, Phys. Rev. Lett. 95, 122501 (2005).
- [20] F. J. Fattoyev, C. J. Horowitz, J. Piekarewicz, and G. Shen, Phys. Rev. C 82, 055803 (2010).
- [21] G. A. Lalazissis, T. Niksić, D. Vretenar, and P. Ring, Phys. Rev. C 71, 024312 (2005).
- [22] X. Roca-Maza, X. Viñas, M. Centelles, P. Ring, and P. Schuck, Phys. Rev. C 84, 054309 (2011).
- [23] S. S. Avancini, S. Chiacchiera, D. P. Menezes, and C. Providência, Phys. Rev. C 82, 055807 (2010).
- [24] M. Centelles, M. Del Estal, X. Viñas, Nucl. Phys. A 635, 193 (1998); M. Del Estal, M. Centelles, X. Viñas, Nucl. Phys. A 650, 443 (1999).
- [25] C. J. Pethick and D. G. Ravenhall, Annu. Rev. Nucl. Part. Sci. 45, 429 (1995).
- [26] D. G. Ravenhall, C. D. Bennett and C. J. Pethick, Phys. Rev. Lett. 28, 978 (1972).
- [27] K. Oyamatsu, Nucl. Phys. A 561, 431 (1993).
- [28] K. Sumiyoshi, K. Oyamatsu and H. Toki, Nucl. Phys. A 595, 327 (1995).
- [29] T. Maruyama, T. Tatsumi, D.N. Voskresensky, T. Tani-

- gawa and S. Chiba, Phys. Rev C, 72, 015802 (2005).
- [30] H. Pais, A. Santos, L. Brito and C. Providência, Phys. Rev. C, 82, 025801 (2010).
- [31] L. Di Gallo, M. Oertel, and M. Urban, Phys. Rev. C, 84, 045801 (2011).
- [32] H. Sonoda, G. Watanabe, K. Sato, T. Takiwaki, K. Yasuoka and T. Ebisuzaki, Phys. Rev. C 75, 042801 (2007).

	ρ_0 [fm^{-3}]	E_0 [MeV]	K_0 [MeV]	E_{sym} [MeV]	L [MeV]	M^*/M	m_σ [MeV]
SLy4	0.159	-15.97	229.8	31.8	45.3	0.695	-
NL3	0.148	-16.24	270.7	37.3	118.3	0.600	508.2
DD-ME2	0.152	-16.14	250.8	32.3	51.4	0.609	550.0
DD-ME δ	0.152	-16.12	219.1	32.4	52.9	0.572	566.2
NL3 $_{\omega\rho}$	0.148	-16.30	272.0	31.7	55.2	0.600	508.2
FSU	0.148	-16.30	230.0	32.6	60.5	0.620	491.5
IU-FSU	0.155	-16.40	231.2	31.3	47.2	0.620	491.5

TABLE I: Nuclear matter properties at the saturation density (density, binding energy, incompressibility, symmetry energy, symmetry energy slope and effective mass) and the σ meson mass.

Regions	1	2	3	4	5	6	7	8	9	10	11	12
ρ [10^{-3}fm^{-3}]	47.1	20.2	8.83	5.72	3.70	1.58	0.871	0.595	0.396	0.276	0.259	0.188
Z												
HFB	-	40	54	40	46	50	50	36	38	36	38	38
N&V	40	50	50	50	50	40	40	40	40	40	-	-
NL3	16	27	32	34	36	38	38	39	39	39	39	39
DD-ME2	33	39	42	43	43	43	43	43	43	42	43	42
DD-ME δ	32	39	42	42	42	42	41	41	41	41	41	40
NL3 $_{\omega\rho}$	39	42	44	44	44	44	44	44	43	43	43	42
FSU	37	44	46	46	46	46	46	46	45	45	45	44
IU-FSU	82 ^r	63	54	52	50	48	47	47	47	46	46	45
N												
HFB	-	1018	1324	732	740	454	316	174	120	82	82	82
N&V	1460	1750	1300	1050	900	460	280	210	160	140	-	-
NL3	1019	1816	1202	925	718	410	259	193	134	98	96	89
DD-ME2	1116	1463	1213	1016	808	482	313	229	160	110	106	92
DD-ME δ	1107	1301	1087	908	739	448	286	211	147	105	99	86
NL3 $_{\omega\rho}$	1300	1590	1291	1045	821	476	308	224	152	108	102	92
FSU	1192	1482	1243	1035	835	503	328	241	164	116	110	96
IU-FSU	1655 ^r	1417	1188	1031	840	510	332	247	173	120	113	95
R_{ws} [fm]												
HFB	-	23.2	33.4	31.8	37.0	42.4	46.4	43.8	45.6	46.8	48.0	53.4
N&V	19.6	27.6	33.1	35.7	39.3	42.2	44.3	46.3	49.2	53.6	-	-
NL3	17.4	27.9	32.2	34.2	36.5	40.8	43.3	45.3	47.1	49.1	49.9	54.6
DD-ME2	18.0	26.1	32.4	35.4	38.0	43.0	46.0	47.8	49.6	50.8	51.6	55.5
DD-ME δ	17.9	25.1	31.3	34.1	36.9	42.0	44.8	46.6	48.4	50.1	50.5	54.3
NL3 $_{\omega\rho}$	18.9	26.8	33.0	35.7	38.2	42.9	45.9	47.6	49.0	50.7	51.1	55.5
FSU	18.4	26.2	32.7	35.6	38.5	43.7	46.8	48.7	50.1	51.8	52.3	56.3
IU-FSU	19.8 ^r	26.0	32.3	35.6	38.6	43.9	47.0	49.1	51.0	52.3	52.7	56.3

TABLE II: Cell proton number, neutron number and Wigner-Seitz radius for different nuclear interactions at the considered densities. HFB and N&V refer respectively to the results found in [9] and [1]. In the region 1, for the IU-FSU interaction, the cell shape is the rod.

Regions	1	2	3	4	5	6	7	8	9	10	11	12
ρ [10^{-3}fm^{-3}]	47.1	20.2	8.83	5.72	3.70	1.58	0.871	0.595	0.396	0.276	0.259	0.188
E/A [MeV]												
HFB	—	4.747	3.025	2.283	1.645	0.612	-0.051	-0.490	-1.063	-1.691	-1.830	-2.441
N&V	6.428	4.097	2.610	1.996	1.465	0.541	-0.050	-0.462	-0.962	-1.425	—	—
NL3	4.491	3.054	2.438	2.096	1.735	0.993	0.422	-0.004	-0.545	-1.130	-1.244	-1.801
DD-ME2	6.847	4.494	3.130	2.560	2.051	1.174	0.584	0.170	-0.341	-0.890	-1.002	-1.581
DD-ME δ	6.986	4.796	3.313	2.681	2.123	1.186	0.569	0.139	-0.391	-0.959	-1.075	-1.666
NL3 $_{\omega\rho}$	6.750	4.354	3.020	2.474	1.984	1.122	0.526	0.100	-0.430	-1.003	-1.119	-1.702
FSU	6.987	4.660	3.202	2.601	2.072	1.173	0.575	0.155	-0.362	-0.917	-1.030	-1.609
IU-FSU	8.531	5.630	3.645	2.884	2.252	1.250	0.623	0.194	-0.325	-0.881	-0.994	-1.587
μ_N [MeV]												
HFB	—	7.178	4.600	3.713	3.117	1.730	1.036	0.724	0.327	-2.660	-3.278	-3.287
N&V	10.900	6.500	4.200	3.300	2.600	1.400	1.000	0.600	0.300	0.200	—	—
NL3	7.285	3.242	2.550	2.261	1.932	1.253	0.816	0.556	0.288	-0.031	-0.189	-0.809
DD-ME2	10.118	5.842	3.883	3.147	2.511	1.509	0.971	0.677	0.398	0.145	0.094	-0.442
DD-ME δ	9.717	6.218	4.224	3.394	2.679	1.572	0.995	0.689	0.397	0.144	0.094	-0.515
NL3 $_{\omega\rho}$	10.050	5.712	3.715	3.009	2.409	1.455	0.935	0.646	0.365	0.105	0.046	-0.568
FSU	9.938	6.130	4.040	3.244	2.569	1.526	0.974	0.677	0.390	0.133	0.086	-0.526
IU-FSU	11.659	7.907	4.933	3.822	2.934	1.671	1.051	0.731	0.432	0.179	0.131	-0.425
x												
HFB	—	0.038	0.039	0.052	0.059	0.099	0.137	0.171	0.241	0.305	0.317	0.317
N&V	0.027	0.028	0.037	0.045	0.053	0.080	0.125	0.160	0.200	0.222	—	—
NL3	0.015	0.015	0.026	0.035	0.048	0.085	0.128	0.168	0.225	0.285	0.289	0.305
DD-ME2	0.029	0.026	0.033	0.041	0.051	0.082	0.121	0.158	0.212	0.276	0.289	0.313
DD-ME δ	0.028	0.029	0.037	0.044	0.054	0.086	0.125	0.163	0.218	0.281	0.293	0.317
NL3 $_{\omega\rho}$	0.029	0.026	0.033	0.040	0.051	0.085	0.125	0.164	0.221	0.285	0.297	0.313
FSU	0.030	0.029	0.036	0.043	0.052	0.084	0.123	0.160	0.215	0.280	0.290	0.314
IU-FSU	0.047	0.043	0.043	0.048	0.056	0.086	0.124	0.160	0.214	0.277	0.289	0.321

TABLE III: Cell energy per baryon, neutron chemical potential and proton fraction for several nuclear interactions at the considered densities. HFB and N&V refer respectively to the results found in [9] and [1]. In the region 1, for the IU-FSU interaction, the cell shape is the rod.

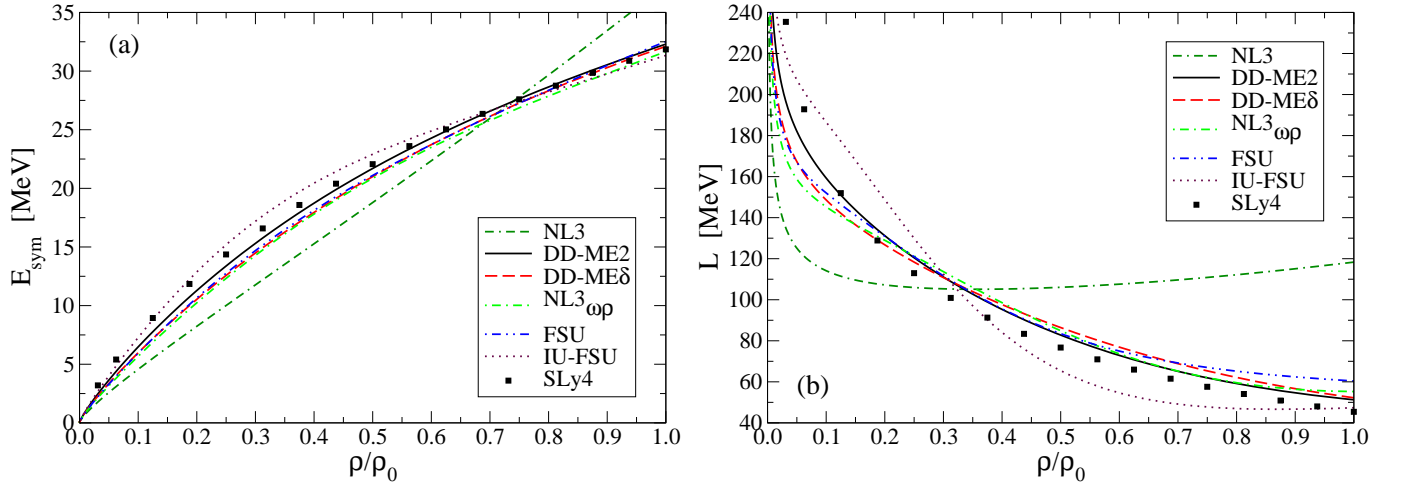


FIG. 1: (Colors online) Symmetry energy E_{sym} (a) and its slope L (b) as a function of the density ρ .

ρ [fm ⁻³]	Z						N					
	NL3	DD-ME2	DD-ME δ	NL3 $_{\omega\rho}$	FSU	IU-FSU	NL3	DD-ME2	DD-ME δ	NL3 $_{\omega\rho}$	FSU	IU-FSU
8.94×10^{-2}				–		–				–		–
8.88×10^{-2}				–		173				–		3594
8.35×10^{-2}				–		117				–		2418
8.29×10^{-2}				67		114				1680		2355
7.82×10^{-2}	–	–	–	60	–	101	–	–	–	1557	–	2071
7.66×10^{-2}	–	–	–	59	–	99	–	–	–	1548	–	2027
7.51×10^{-2}	–	–	49	59	–	97	–	–	1396	1565	–	1981
7.35×10^{-2}	–	–	48	49	56	95	–	–	1385	1319	1503	1935
7.20×10^{-2}	–	54	47	47	53	94	–	1467	1373	1280	1439	1910
7.04×10^{-2}	–	51	37	46	51	93	–	1403	1095	1267	1401	1885
6.88×10^{-2}	–	50	36	45	50	92	–	1394	1079	1254	1391	1861
6.73×10^{-2}	–	41	35	45	50	92	–	1158	1061	1269	1407	1856
6.57×10^{-2}	–	39	35	44	41	91	–	1116	1074	1255	1170	1833
6.42×10^{-2}	–	38	35	44	40	91	–	1102	1086	1271	1153	1830
6.26×10^{-2}	–	38	35	42	40	90	–	1115	1099	1232	1167	1807
6.11×10^{-2}	–	38	31	41	39	99	–	1131	986	1218	1150	1997
5.95×10^{-2}	–	34	31	40	39	96	–	1029	997	1203	1161	1934
5.79×10^{-2}	–	33	31	40	40	94	–	1012	1008	1218	1203	1892
5.64×10^{-2}	–	33	31	40	37	92	–	1026	1018	1233	1128	1851
5.48×10^{-2}	–	32	31	40	37	89	–	1009	1028	1249	1139	1789
5.33×10^{-2}	13	32	31	39	37	87	737	1024	1038	1234	1150	1749
5.17×10^{-2}	13	32	31	39	37	86	759	1038	1047	1249	1161	1730
5.02×10^{-2}	14	33	32	39	37	85	843	1085	1090	1267	1171	1711
4.86×10^{-2}	15	33	32	39	37	83	929	1100	1099	1283	1182	1672
4.71×10^{-2}	16	33	32	39	37	82	1019	1116	1107	1300	1192	1655

TABLE IV: Proton and neutron number in the pasta phase region for several nuclear interactions. The horizontal lines represent the shape transitions, droplet-rod, rod-slab and slab-core. For NL3 only the droplet-core transition occurs, and for IU-FSU the droplet-rod transition occurs at the lowest density shown.

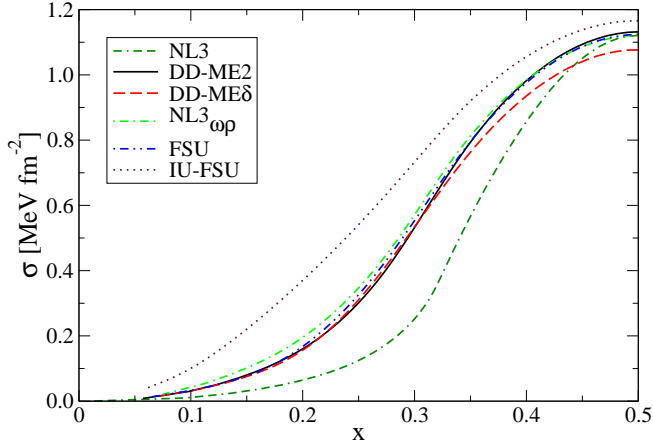


FIG. 2: (Colors online) Surface tension as a function of the proton fraction x for all the models considered in this study except SLy4.

ρ [fm ⁻³]	R_w [fm]						E/A [MeV]					
	NL3	DD-ME2	DD-ME δ	NL3 $_{\omega\rho}$	FSU	IU-FSU	NL3	DD-ME2	DD-ME δ	NL3 $_{\omega\rho}$	FSU	IU-FSU
8.94×10^{-2}				–		–				10.043		10.945
8.88×10^{-2}				–		23.6				10.000		10.922
8.35×10^{-2}				–		16.9				9.614		10.693
8.29×10^{-2}				11.7		16.5				9.570		10.667
7.82×10^{-2}	9.2	12.0	10.5	11.5	16.1	15.4	7.512	9.351	9.167	9.217	9.241	10.448
7.66×10^{-2}	8.0	13.0	7.0	11.7	2.0	15.4	7.324	9.230	9.060	9.100	9.130	10.373
7.51×10^{-2}	8.8	11.0	10.7	12.0	10.2	15.4	7.141	9.110	8.951	8.983	9.021	10.296
7.35×10^{-2}	9.3	10.0	10.8	14.1	11.8	15.3	6.961	8.989	8.842	8.865	8.913	10.217
7.20×10^{-2}	7.9	11.7	11.0	14.0	11.5	15.5	6.786	8.868	8.734	8.746	8.802	10.137
7.04×10^{-2}	8.9	11.5	13.1	14.1	11.5	15.6	6.614	8.745	8.626	8.627	8.691	10.055
6.88×10^{-2}	8.4	11.7	13.1	14.1	11.6	15.8	6.445	8.622	8.517	8.507	8.581	9.972
6.73×10^{-2}	9.0	13.8	13.1	14.4	12.0	16.1	6.281	8.498	8.409	8.386	8.470	9.886
6.57×10^{-2}	9.3	13.7	13.4	14.5	14.0	16.3	6.121	8.373	8.300	8.264	8.359	9.798
6.42×10^{-2}	8.7	13.7	13.6	14.7	14.0	16.6	5.964	8.248	8.192	8.142	8.248	9.708
6.26×10^{-2}	9.4	14.0	13.9	16.9	14.3	16.8	5.812	8.123	8.083	8.019	8.136	9.616
6.11×10^{-2}	9.3	14.3	15.8	17.0	14.4	19.1	5.664	7.998	7.974	7.896	8.024	9.522
5.95×10^{-2}	9.6	16.2	16.0	17.1	14.6	19.0	5.519	7.871	7.866	7.771	7.911	9.423
5.79×10^{-2}	9.9	16.3	16.2	17.3	15.1	19.1	5.379	7.745	7.757	7.646	7.798	9.322
5.64×10^{-2}	19.3	16.5	16.4	17.5	17.0	19.1	5.241	7.617	7.647	7.520	7.685	9.219
5.48×10^{-2}	20.6	16.5	16.6	17.8	17.2	19.1	5.108	7.490	7.538	7.394	7.570	9.112
5.33×10^{-2}	15.0	16.8	16.9	17.9	17.5	19.1	4.977	7.362	7.429	7.266	7.455	9.003
5.17×10^{-2}	15.3	17.0	17.1	18.1	17.7	19.3	4.850	7.234	7.319	7.138	7.339	8.890
5.02×10^{-2}	16.0	17.5	17.5	18.4	17.9	19.5	4.726	7.105	7.208	7.010	7.223	8.774
4.86×10^{-2}	16.7	17.7	17.7	18.7	18.2	19.6	4.606	6.976	7.097	6.880	7.105	8.654
4.71×10^{-2}	17.4	18.0	17.9	18.9	18.4	19.8	4.491	6.847	6.986	6.750	6.987	8.531

TABLE V: Cell Wigner-Seitz radius and energy per baryon in the pasta phase region. The horizontal lines represent the shape transitions, droplet-rod, rod-slab and slab-core. For NL3 only the droplet-core transition occurs, and for IU-FSU the droplet-rod transition occurs at the lowest density shown.

ρ [fm ⁻³]	μ_N [MeV]						x					
	NL3	DD-ME2	DD-ME δ	NL3 $_{\omega\rho}$	FSU	IU-FSU	NL3	DD-ME2	DD-ME δ	NL3 $_{\omega\rho}$	FSU	IU-FSU
8.94×10^{-2}				15.930		13.711				0.040		0.045
8.88×10^{-2}				15.837		13.941				0.040		0.045
8.35×10^{-2}				15.006		13.752				0.038		0.046
8.29×10^{-2}				15.049		13.730				0.038		0.046
7.82×10^{-2}	16.359	14.759	13.924	14.419	14.150	13.529	0.029	0.037	0.035	0.037	0.037	0.047
7.66×10^{-2}	15.800	14.518	13.672	14.207	13.876	13.460	0.028	0.037	0.034	0.037	0.037	0.047
7.51×10^{-2}	15.250	14.278	13.534	13.995	13.613	13.387	0.027	0.036	0.034	0.036	0.036	0.047
7.35×10^{-2}	14.712	14.037	13.310	13.822	13.473	13.312	0.027	0.036	0.033	0.036	0.036	0.047
7.20×10^{-2}	14.180	13.867	13.084	13.613	13.255	13.235	0.026	0.036	0.033	0.035	0.036	0.047
7.04×10^{-2}	13.661	13.641	12.891	13.402	13.034	13.155	0.025	0.035	0.033	0.035	0.035	0.047
6.88×10^{-2}	13.154	13.412	12.673	13.189	12.814	13.073	0.024	0.035	0.032	0.035	0.035	0.047
6.73×10^{-2}	12.654	13.216	12.454	12.976	12.595	12.989	0.023	0.034	0.032	0.034	0.034	0.047
6.57×10^{-2}	12.166	12.987	12.236	12.759	12.417	12.902	0.023	0.034	0.032	0.034	0.034	0.047
6.42×10^{-2}	11.687	12.756	12.019	12.543	12.204	12.813	0.022	0.033	0.031	0.033	0.034	0.047
6.26×10^{-2}	11.219	12.521	11.803	12.338	11.996	12.718	0.021	0.033	0.031	0.033	0.033	0.047
6.11×10^{-2}	10.763	12.287	11.597	12.119	11.785	12.679	0.020	0.033	0.030	0.033	0.033	0.047
5.95×10^{-2}	10.318	12.064	11.384	11.896	11.575	12.584	0.020	0.032	0.030	0.032	0.033	0.047
5.79×10^{-2}	9.884	11.825	11.172	11.673	11.368	12.485	0.019	0.032	0.030	0.032	0.032	0.047
5.64×10^{-2}	9.479	11.585	10.960	11.447	11.172	12.382	0.018	0.031	0.030	0.031	0.032	0.047
5.48×10^{-2}	9.087	11.344	10.750	11.219	10.966	12.274	0.018	0.031	0.029	0.031	0.031	0.047
5.33×10^{-2}	8.752	11.102	10.541	10.990	10.760	12.162	0.017	0.030	0.029	0.031	0.031	0.047
5.17×10^{-2}	8.370	10.857	10.333	10.757	10.555	12.045	0.017	0.030	0.029	0.030	0.031	0.047
5.02×10^{-2}	7.999	10.612	10.127	10.524	10.349	11.922	0.016	0.030	0.029	0.030	0.031	0.047
4.86×10^{-2}	7.637	10.365	9.922	10.288	10.144	11.793	0.016	0.029	0.028	0.030	0.030	0.047
4.71×10^{-2}	7.285	10.118	9.717	10.050	9.938	11.659	0.015	0.029	0.028	0.029	0.030	0.047

TABLE VI: Neutron chemical potential and proton fraction in the pasta phase region. The horizontal lines represent the shape transitions, droplet-rod, rod-slab and slab-core. For NL3 only the droplet-core transition occurs, and for IU-FSU the droplet-rod transition occurs at the lowest density shown.

Transition	SLy4(HF)	SLy4(TF)	NL3	DD-ME2	DD-ME δ	NL3 $_{\omega\rho}$	FSU	IU-FSU
droplet - rod	0.042	0.066	-	0.0611	0.0626	0.0642	0.0580	0.0471
rod - slab	0.070	0.078	-	0.0688	0.0720	0.0751	0.0673	0.0626
slab - homogeneous	0.080	0.085	0.0548*	0.0735	0.0766	0.0835	0.0751	0.0894

TABLE VII: Densities at the shape transition. The densities are give in fm⁻³. SLy4(HF) and SLy4(TF) refer to the results found in [7]. For NL3, only the transition droplet-core is indicated.

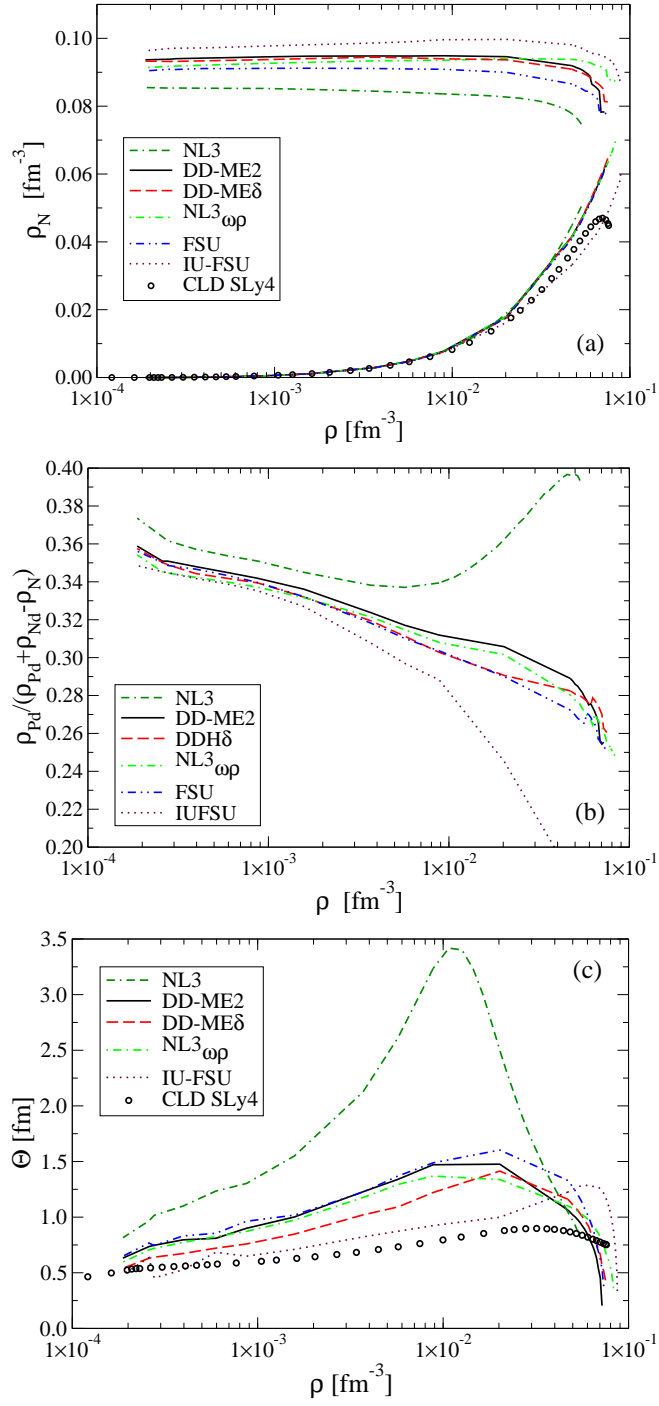


FIG. 3: (Colors online) Neutron density at the cell center and border (a), cluster proton fraction at the cluster center (b) and neutron skin thickness (c) for all the models considered in this study.

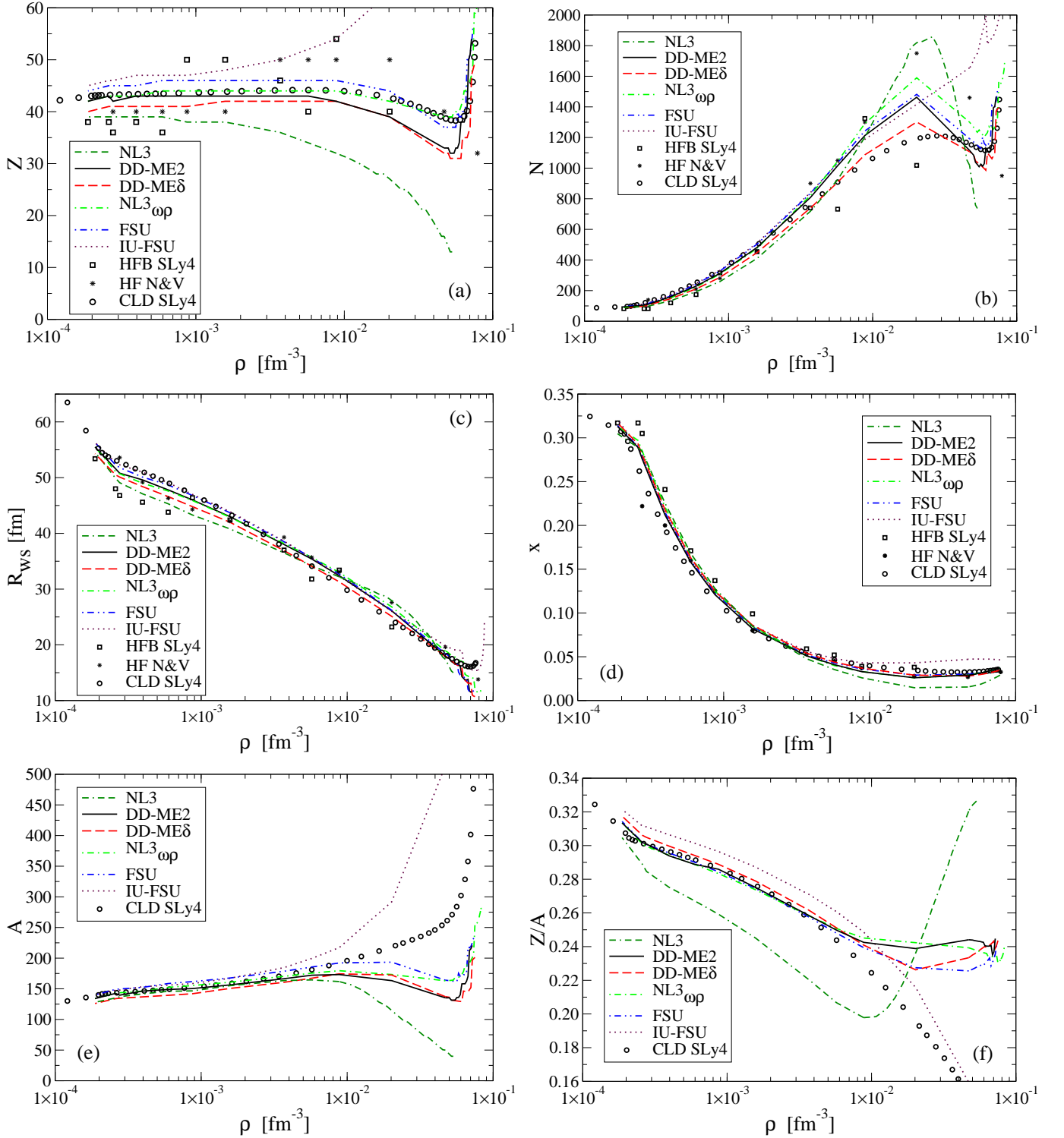


FIG. 4: (Colors online) Proton number Z (a), neutron number N (b), Wigner-Seitz cell radius R_{ws} (c), proton fraction x (d), the baryon number in the nucleus A (e) and the proton fraction in the nucleus Z/A (f) as a function of the density (ρ). HFB SLy4, HF N&V and CLD SLy4 refer respectively to the results found in [9], [1] and [3].

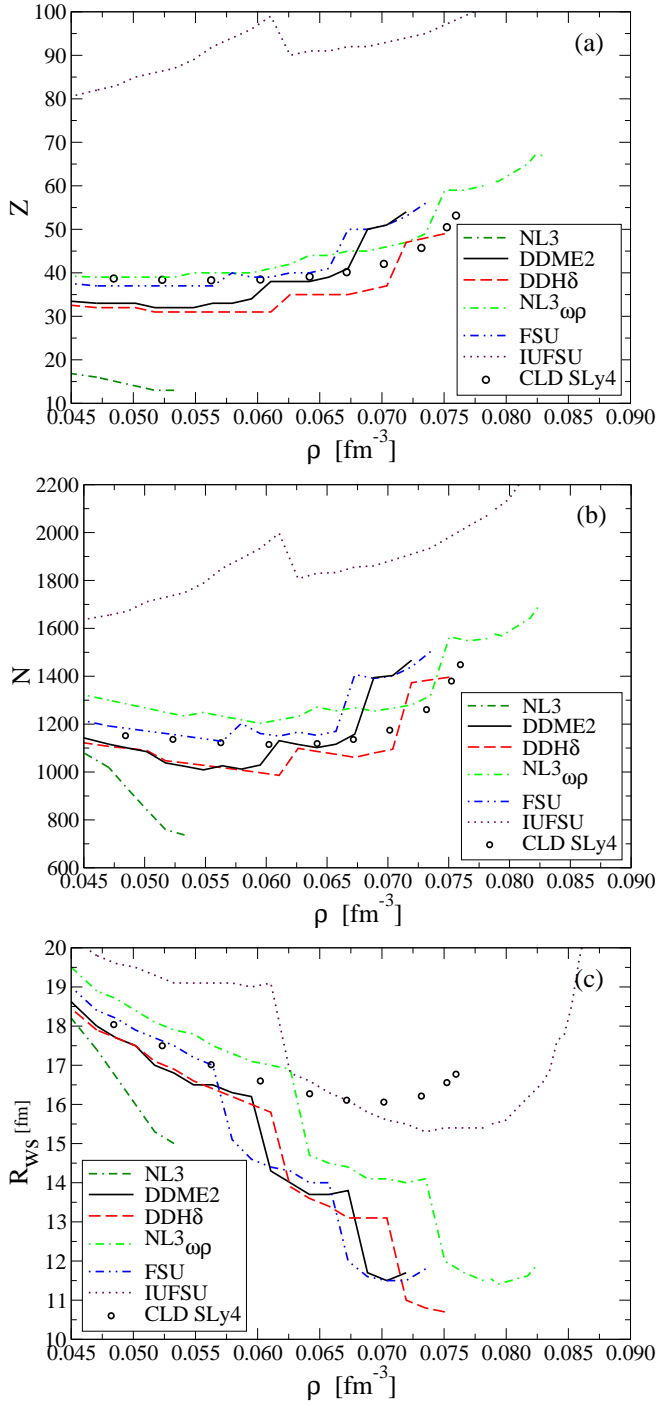


FIG. 5: (Colors online) Proton number (a), neutron number (b) and Wigner-Seitz cell radius (c) in the pasta phase regions. CLD *SLy4* refers to the results found in [3].